INL/RPT-24-79322

Demonstration of Temperature Compensation Techniques for SPNDs Operating in High Temperatures

Advanced Sensors and Instrumentation

Milestone Report—M3CT-24IN0702012

JUNE 2024

Kevin Tsai

Idaho National Laboratory

Idaho National Laboratory

Battelle Energy Alliance manages INL for the U.S. Department of Energy's Office of Nuclear Energy

INL/RPT-24-79322

Demonstration of Temperature Compensation Techniques for SPNDs Operating in High Temperatures

Milestone Report—M3CT-24IN0702012

Kevin Tsai

JUNE 2024

Idaho National Laboratory
Idaho Falls, Idaho 83415

http://www.inl.gov

Prepared for the
U.S. Department of Energy
Office of Energy
Under DOE Idaho Operations Office
Contract DE-AC07-05ID14517

Page intentionally left blank

ABSTRACT

This report presents the testing results of rhodium-based self-powered neutron detectors (Rh-SPND) irradiated in a furnace dry tube from ambient temperature to 850°C at the Ohio State University Research Reactor (OSURR).

The purpose of the experiment was to demonstrate the technique and application of a temperature compensation method for the Rh–SPND. This was performed by characterizing the temperature effects observed in past experiments—a displacement current and a stabilized dark current—of the Rh–SPND as a function of temperature under the models of shifting space charges as a product of photoconductivity properties. Low-power irradiation was performed at the OSURR with stabilized temperatures of ambient, 550, 575, 600, 625, 650, 675, and 700°C to obtain the curve fit parameters that describes the temperature effects.

The results provided further insight for the behavior of the SPND at high temperatures in accordance with available insulation conductivity models. Transition points from photoconductivity to ionic conductivity were identified in the range of 550–600°C. Additionally, transition points from ionic to electric conductivity were observed in the range of 675–700°C, however, the data was not able to fully capture the transition and did not have enough resolution to provide predictive compensation based only on temperature readings.

Page intentionally left blank

ACKNOWLEDGMENTS

The author would like to thank the Ohio State University Research Reactor staff: Matthew Van Zile, Kevin Herminghuysen, Andrew Kauffman, and Susan White for their advice and support for the successful irradiation campaign, with additional thanks to Matthew Van Zile for his contributions in the design, construction, and thermal characterization of the furnace rig used in the experiment.

Page intentionally left blank

CONTENTS

FIGURES

TABLES

ACRONYMS

MCNP	Monte Carlo N-Particle (transport code)
OSURR	Ohio State University Research Reactor
Rh-SPND	Rhodium-based self-powered neutron detector
SPND	Self-powered neutron detector

Page intentionally left blank

Demonstration of Temperature Compensation Techniques for SPNDs Operating in High Temperatures

1. INTRODUCTION

In the commercial nuclear industry, reactor power monitoring is performed with the combined use of in-core (built-in assembly or traversing in-core) and ex-core (out-of-vessel) detectors that measure the intensity of neutron and gamma flux or reactor power. The dual implementation of in-core and ex-core detectors is common in the nuclear industry, with very few exceptions. While ex-core detectors are used for power monitoring and control, in-core detectors are often needed for power distribution mapping to verify power peaking factors are within technical specifications, calibrate ex-core detectors, and increase the margin of operation. [1], [2]

Under the Advanced Reactor Demonstration Program supported by the U.S. Department of Energy, a multitude of advanced reactor designs are expected to be built and tested. Many of these designs are expected to operate at higher inlet temperatures near 650°C and above for increased thermal efficiency and heat process applications. [3] While the higher operating temperatures boast an increase in thermal efficiency and utilization, they significantly limit the availability of in-core and near-core detectors.

Self-powered neutron detectors (SPND) have many advantages as an in-core detector. Its construction is simple and robust—taking the form of a mineral-insulated, metal-sheathed cable with the lead wire attached to a neutron sensitive wire called the emitter. The emitter passively generates an electric current in the radiation field proportional to the neutron field strength resulting in a simple readout system without the need for a high voltage power supply. The material composition and fabrication process of many SPNDs have temperature compatibility of up to 900°C. The omission of a high voltage power supply makes the detector less susceptible to leakage current damage. These qualities make the SPND a candidate for high-temperature reactor applications. [4] However, in practice, both recent experiments and historical records have identified temperature effects for SPNDs operating above 500°C. [4], [6], [7] The two observed temperature effects are a changing steady-state dark current, and a temporary displacement current.

Mitel'man [7] provided a theory with calculated results based on empirical measurements that matched closely with the observed effects. However, the results Mitel'man obtained were specific to the SPND used, and thus this work seeks to apply similar methodologies to the current rhodium-based SPND (Rh–SPND) designs. Two Rh–SPNDs were chosen for the characterization and demonstration of a temperature compensation technique. The heated irradiation was performed in a furnace-rigged dry-tube at the Ohio State University Research Reactor (OSURR).

2. THEORY

SPNDs generate an electric current in a radiation field through neutron and gamma interactions in the emitter, causing a net flow of electrons out of the emitter and into the sheath. The dominant type of neutron-induced current from the emitter dictates the operational mode of the SPND, categorized as delayed-response and prompt-response. Delayed-response SPNDs primarily generate their electric current through neutron activation and subsequent beta-particle decay (n, β^-) interactions; therefore, the response time is dictated by the half-life decay of the activation isotope. Prompt-response SPNDs primarily generate their electric current by two-step interactions of neutron-capture gamma emission, and subsequent photoelectric or Compton scattering emission of electrons (n, γ, e). [8] For the Rh–SPND, the dominant interaction is from the neutron activation of rhodium-103 and subsequent beta-particle decay. As such, the Rh–SPND is categorized as a delayed-response type since the emission of electrons in response to a neutron field is dictated by the decay half-life of rhodium-104. However, it is important to

note that despite the dominant interaction dictating each SPND category, both delayed and prompt interactions occur in all SPND components including the insulator and sheath. Additionally, depending on the type of interactions, the electron energy spectrum entering the insulator from the emitter and sheath surfaces can vary significantly. An Monte Carlo N-Particle (MCNP) model can be used with the neutron spectrum provided by OSURR [9] as well as the U-235 fission gamma spectrum [10] to illustrate the electron energy distribution of the Rh–SPND at the insulator boundaries between the emitter and the sheath (Figure 1).

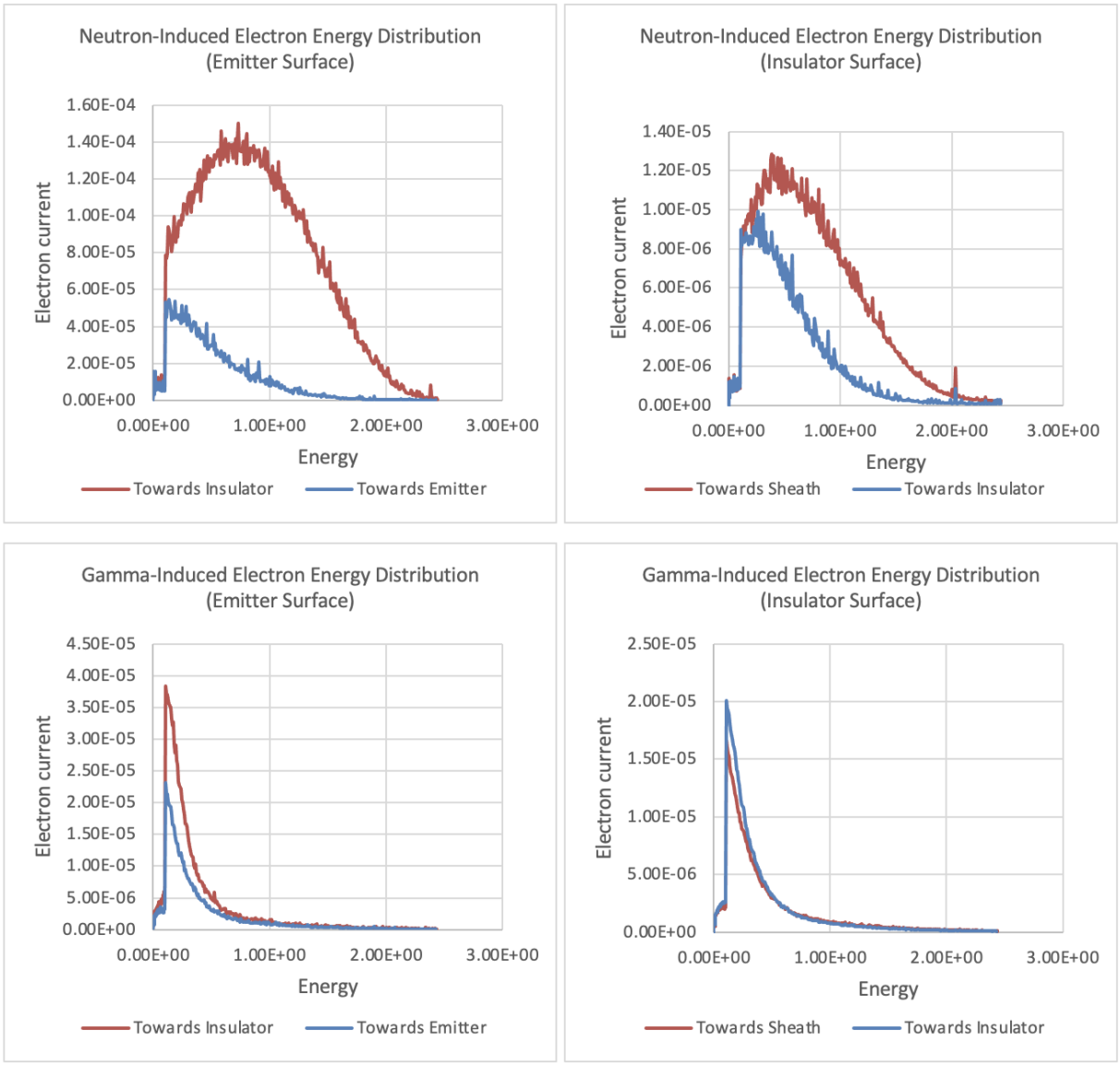

Figure 1. Electron energy distribution at the insulator surfaces at the emitter and sheath.

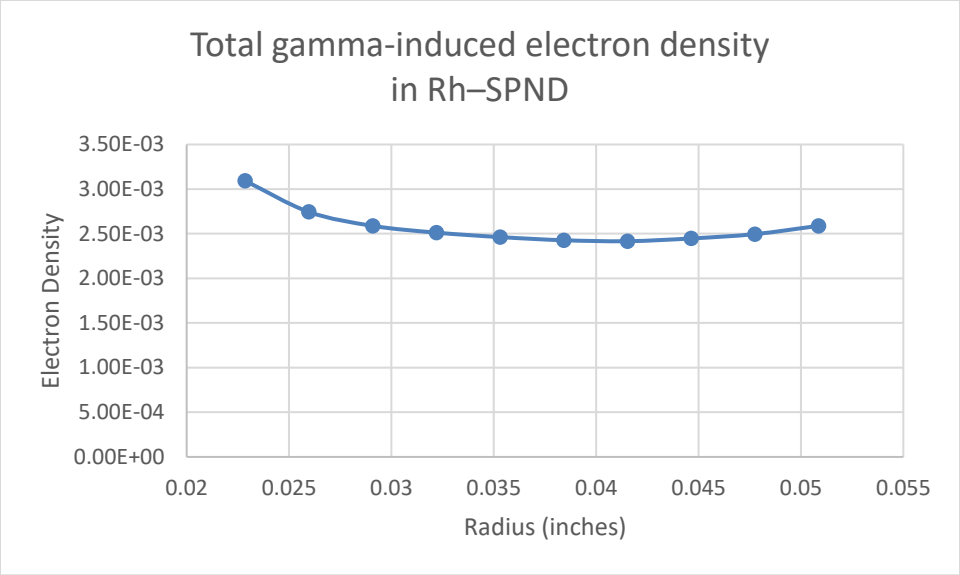

Figure 2. Radial distribution of total gamma-induced electron density.

Given the energy distribution of the emitted electrons, a percentage of them will thermalize within the insulator due to collisions and insufficient kinetic energy. As shown in Figure 1, as well as theorized by Warren, [8] a significant portion of the low-energy electrons is expected to be generated from the external gamma interactions. Additionally, they are expected to be trapped within imperfection or impurity sites of the insulator (it is assumed that this is a significant portion of the total electron density distribution). Figure 2 presents the MCNP results for the gamma-induced electron density distribution as a function of radius, r. This total electron density distribution is used as the main generator of the space charge. The electric field and potential can therefore be calculated by the following equations [11]:

$$E(r) = \frac{1}{\varepsilon r}\left\{\int_{r_e}^{r} r'\rho(r')dr' - \frac{1}{ln\left(\frac{r_s}{r_e}\right)}\int_{r_e}^{r_s} dr'' \frac{1}{r''}\int_{r_e}^{r_s} r'\rho(r')dr'\right\} \quad (1)$$

$$\Delta V = \int_{r_e}^{r} E(r')dr' \quad (2)$$

where

ε = the electric permittivity of the insulator

r_e = the emitter outer radius

r_s = the sheath inner radius.

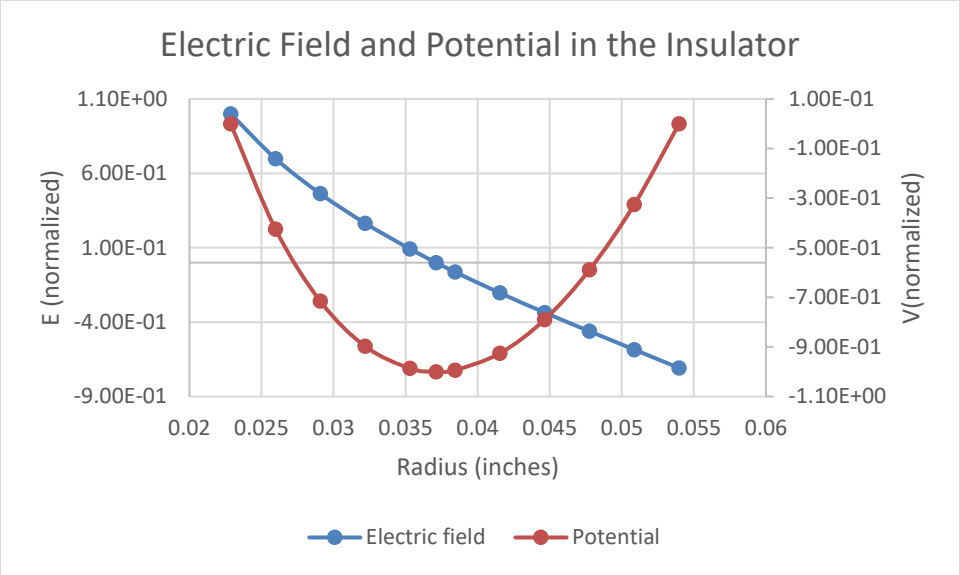

Figure 3. Calculated electric field and potential in the insulator as calculated from Equations (1) and (2) from the radial distribution given in Figure 2.

As shown in Figure 3, the electric potential has one peak, and as theorized by Warren [12], a threshold kinetic energy, E_{MIN}, is needed for the electron to move past the electric potential before thermalizing, coming into the effect of the electric field and moving the thermalized electron to the emitter or sheath, respectively; thus, electrons with energy less than E_{MIN} will not contribute to the electric current while electrons with energy greater than E_{MIN} will.

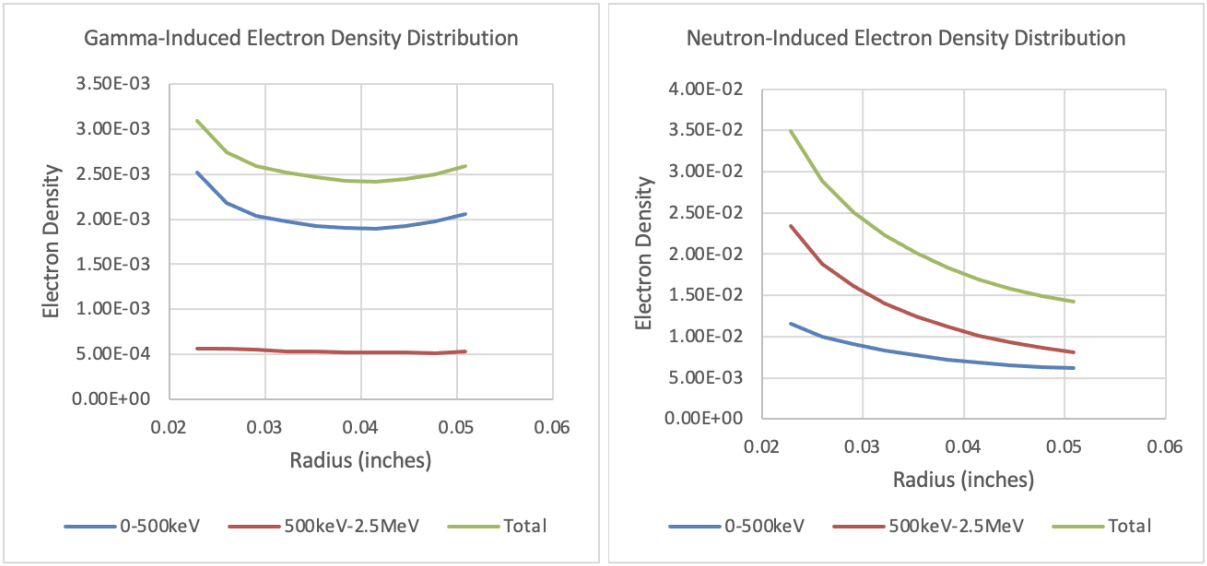

(a) (b)

Figure 4. Neutron and gamma-induced electron density distribution with EMIN bins.

For a qualitative evaluation, using Warren's formalism, E_{MIN} is approximated to be 500 keV. Figure 4(a) re-illustrates the electron density distribution provided in Figure 2 with energy groups above and below E_{MIN}. Additionally, Figure 4 provides the neutron-induced electron density distribution with

the same energy groups. It can be observed from Figure 4(b) that for a neutron-induced electron distribution, which is largely dominated by the (n, β^-) interactions, a larger portion of the electron density is above E_{MIN}. Conversely, when looking at the gamma-induced electron distribution, a significant portion is below E_{MIN}. This fortifies the theory for a significant gamma-contributed space charge and provides the follow-up theory that (n, β^-) contributions and sensitivity will not be affected by temperature, but rather will be superimposed above the observed displacement currents. Additionally, for the temperature compensation method, a low-power or gamma irradiation would suffice in characterizing the temperature effects to a multiplication factor of the gamma intensity.

As discussed above, assuming the space charge is generated with a significant portion of electrons being trapped, an increase in temperature would free the electrons back into the conduction band with density, n_c. This would follow the form of [13]:

$$n_c = ce^{-\frac{\left(\frac{1}{2}E_f\right)}{kT}} \tag{3}$$

Where

c = radiation field intensity

E_f = energy necessary to free the electron from the traps (from imperfections or impurities) to the conduction band

k = Boltzmann constant

T = absolute temperature.

Equation (4) therefore shows the increase in electrons that would follow the space charge potential and eventually be swept out into the emitter and sheath—both shifting the space charge as well as contributing to a displacement current as theorized by Mitel'man. [7] Additionally, with increasing temperatures, the time constant needed for the displacement current (and shifting of the space charge) was found to decrease linearly with a decrease in insulation resistance. [7] The specific properties of the displacement current as well as the steady-state current as a function of temperature are thus related to the imperfections and impurities.

Therefore, this work seeks to characterize the effects of the imperfection and impurity traps at temperature using parameter fits. The displacement current i_T is assumed to be a response function to temperature T with the functional form of

$$i_T(T) = a_1 e^{-a_2/kT} \tag{4}$$

as described in Equation (3). Similarly, as observed and theorized, the relaxation of the discharge current to a base dark current can be described as

$$i_{T=const}(t) = a_3 e^{a_4(t-t_0)} + a_5 \tag{5}$$

Equations (4) and (5) are used to provide the initial fit parameters as they are more easily identified prior to their combined effects of temperature and time decay as provided by Equation (6).

$$i_T(T,t) = a_1 e^{-a_2/kT} e^{a_4(t-t_0)} + a_5 \quad (6)$$

Where the parameters above have the following description:

a_1 is the proportional value related to the field strength as provided by c in Equation (3)

a_2 is the energy necessary to free the electron from the imperfection and impurity sites to the conduction band

a_3 is an initial fitting parameter to Equation (5). It is replaced with $i_T(T)$ in the combined fit given in Equation (6)

a_4 is related to the relaxation time constant. This is expected to increase in magnitude (decreasing decay time-constant) with increasing temperature with a proportionality of $-a_4^{-1} \propto R$ (R=insulator resistance)

a_5 is the expected relaxed steady-state signal at temperature – a dark current. It is related to leakage current as well as low-energy electron emission, however, its behavior in irradiation environments is not well understood.

3. EXPERIMENTAL SETUP

A series of heated irradiations were performed at the OSURR using the 9.5-inch dry tube positioned on the east face of the reactor core. The dry tube was fitted with a 24-inch cylindrical silicon carbide furnace (Figure 5). The two Rh–SPNDs used in this project were identical to inform uniqueness of temperature effects on individual SPNDs. The relevant materials and dimensions of the SPNDs are given in Table 1. Alumina tubes were used as inserts to position the two Rh–SPNDs at axial heights of 2.5 and 6.5 inches from the furnace bottom at the peak nominal flux location, while allowing a 0.5-inch gap between the emitters to reduce the effects of local neutron flux depression or shadowing between the two rhodium emitters. Additionally, a type K thermocouple, denoted TC-1 in the following figures, was placed at the middle of the 0.5-inch emitter gap for measuring temperature effects.

Table 1. Rh–SPND design materials and dimensions.

Emitter	Collector/Sheath	Cable wire
Rhodium (Rh-103) Diameter: 0.457 mm Length: 88.9 mm	Inconel 600 Diameter: 1.57 mm Wall: 0.254 mm	Inconel 600 Diameter: 0.254 mm Length: 7620 mm Insulation: aluminum oxide (Al2O3)

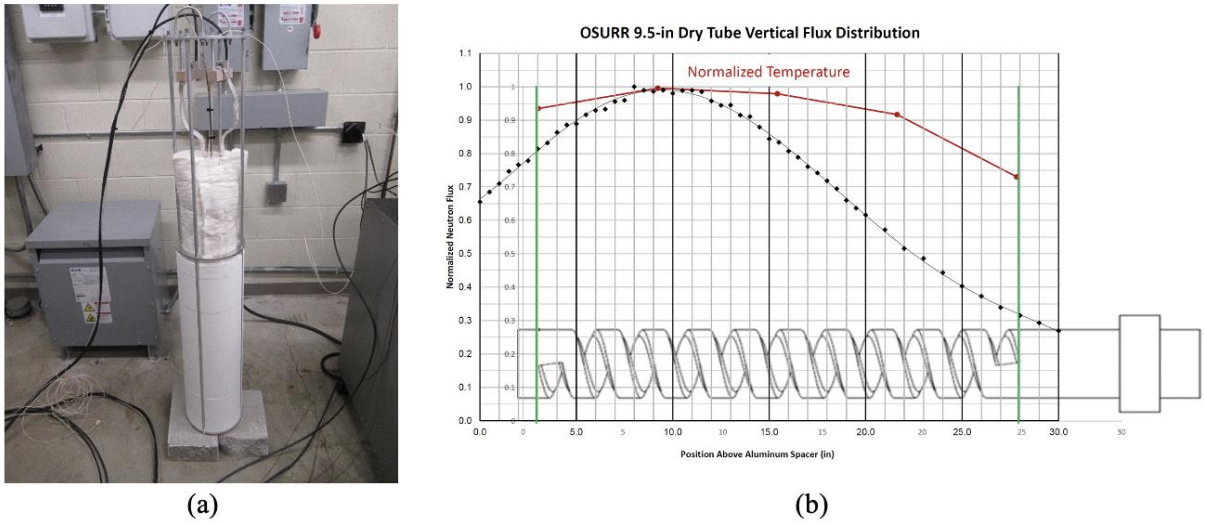

(a) (b)

Figure 5. (a) 24-inch cylindrical silicon carbide furnace (b) with temperature and flux distribution in reference to furnace bottom (green line) as 0-position.

Three irradiation tests were performed. The target power, temperature, and duration are provided in Table 2. The purpose of the first test was to measure the temperature-dependent characteristics at near-zero power (10–30W). Given the targeted temperatures of operation, the heater was operated between temperatures of 550–700°C in 25°C intervals. The goal was to measure the instantaneous signal change, signal stabilization time-constant, and stabilized signal functions of temperature. The following two tests were to provide reactor power changes and test the reproducibility of the temperature effects with sufficient SPND signal generation and the associated temperature compensation method.

Table 2. Irradiation plan with temperature and reactor power demands.

Test 1			Test 2			Test 3		
Power	Hold Duration	Temperature	Power	Hold Duration	Temperature	Power	Hold Duration	Temperature
10-30W	30 min each	Ambient 550°C 575°C 600°C 625°C 650°C 675°C 700°C	100 W	1 hour	Ambient	100 W	1 hour	Ambient
			1 kW 10 kW 100 kW	15 min each	Ambient	1 kW 10 kW 100 kW	15 min each	Ambient
			1 kW	Raise temperature 350°C		1 kW	Raise temperature 700°C	
			1 kW 10 kW 100 kW	15 min each	350°C	1 kW 10 kW 100 kW	15 min each	700°C
			1 kW	Raise temperature 600°C		1 kW	Raise temperature 850°C	
			1 kW 10 kW 100 kW	15 min each	600°C	1 kW 10 kW 100 kW	15 min each	850°C
			1kW	30min each	625°C 650°C			

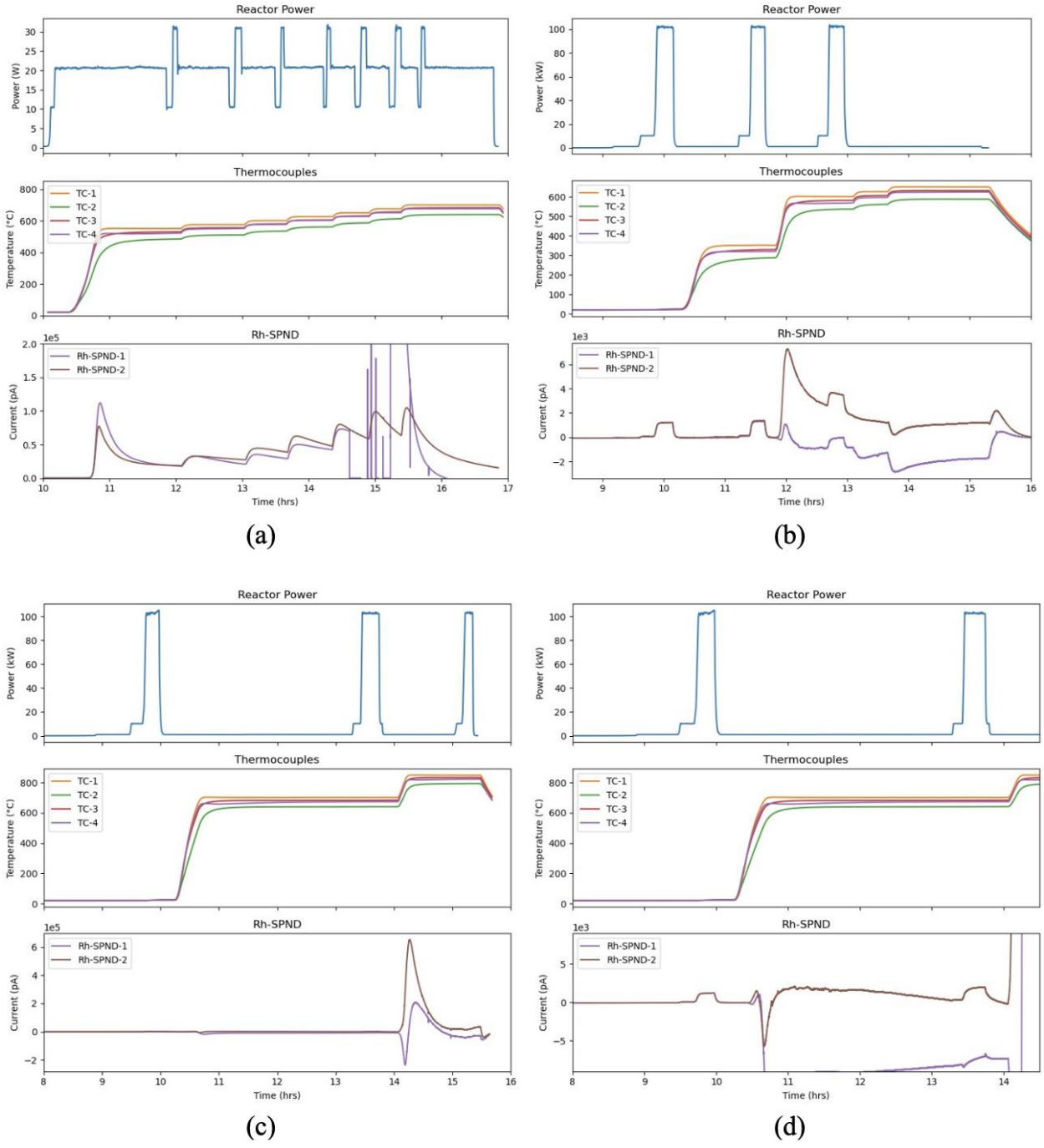

Figure 6. Rh–SPND performance overview for (a) Test 1, (b) Test 2, (c) Test 3, and (d) a magnified view of Test 3.

4. RESULTS

An overview of the Rh–SPND performance across the three irradiation tests is given in Figure 6 with Figure 6(d) as a magnified view of Test 3 at 700°C. As a primary result, it can be observed from Test 2 irradiation that the (n, β^-) does superimpose above the displacement currents at the 11.5 and 12.5-hour mark (Figure 6[b]). However, from the results of Test 3 at the 13.5-hour mark (Figure 6[d])]), a change

in sensitivity and response time of the (n, β^-) contribution was observed. This occurred near 700°C and may have been a result of a change in conductivity described in later sections.

Separately, to characterize the temperature effects, the seven heat-and-hold segments performed in Test 1 were separated based on the local minimum of the signal response (Figure 7). Due to the irregularity in the detector labeled Rh–SPND-1, following the resistance measurement only the response characteristics for the detector labeled Rh–SPND-2 were measured.

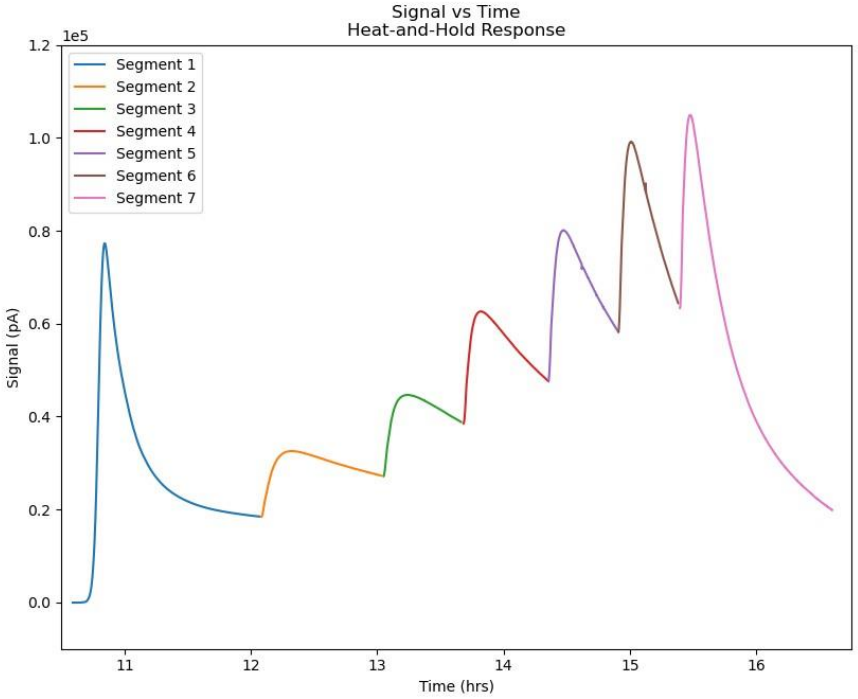

Figure 7. Rh–SPND performance separated into seven segments of heat-and-holds.

Overlayed plots of SPND response for heating are provided in Figure 8. The initial heating to 550°C is on a different scale and is separated in Figure 8(b). Similarly, the overlayed plots of SPND response for steady-state temperature are provided in Figure 9. The relaxation characteristic following the initial heat-up to 550°C is also separated in Figure 9(b). Table 3 contains all the initial fit parameters as provided by Equations (4) and (5).

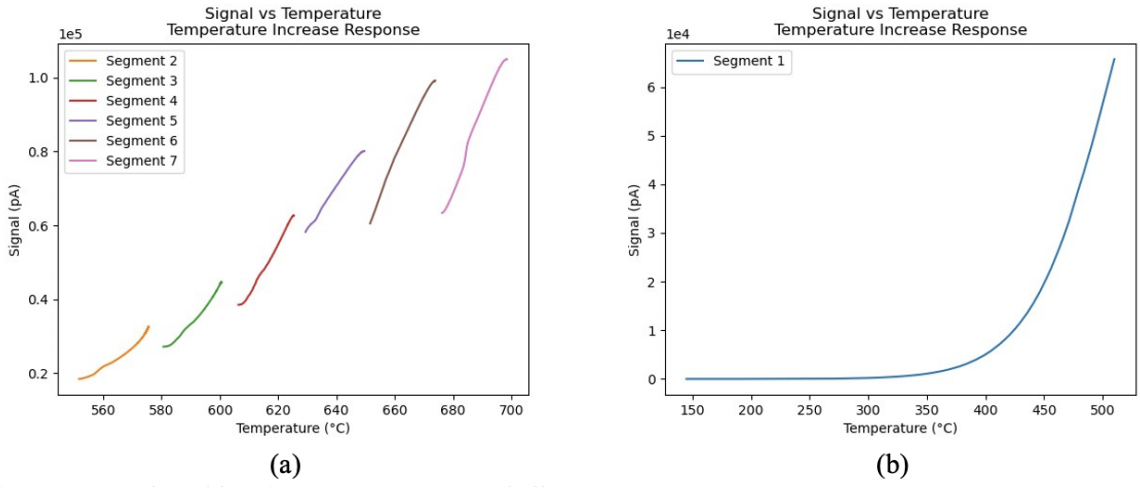

Figure 8. Overlayed heating response curve of all seven segments.

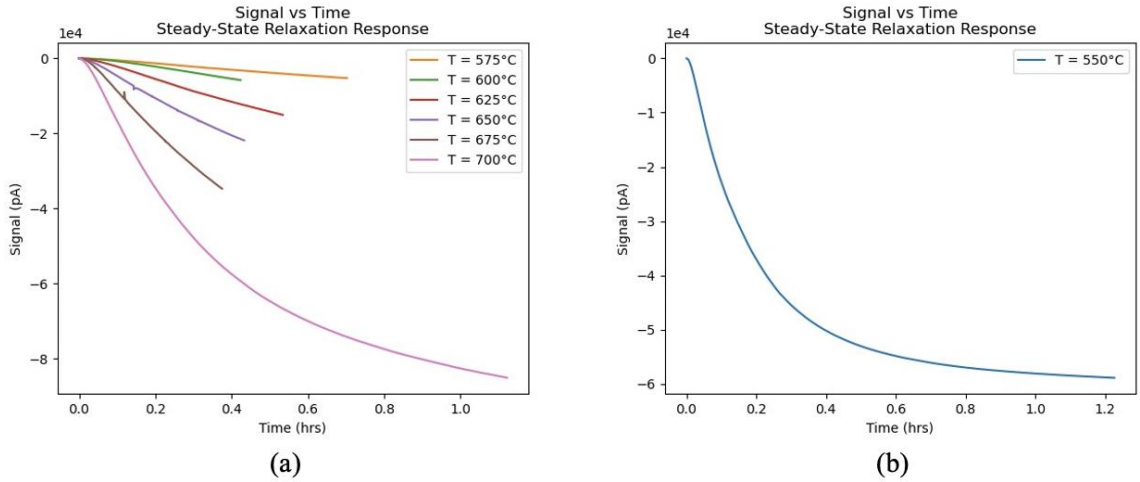

Figure 9. Overlayed steady-state relaxation curve for all seven segments.

Table 3. Fitting parameters $a_{1\text{-}5}$ for Equations (4) and (5) for all seven segments.

Segment	a_1	a_2	a_3	a_4	a_5
1	2.37E+11	1.02E+00	3.30E+04	-4.75E+00	1.89E+04
2	1.14E+14	1.61E+00	4.68E+04	-1.83E-01	-1.39E+04
3	9.36E+14	1.79E+00	-7.91E+03	1.38E+00	5.29E+04
4	2.09E+15	1.88E+00	1.01E+05	-3.24E-01	-3.72E+04
5	1.12E+11	1.12E+00	8.18E+04	-7.70E-01	-6.32E+02
6	1.35E+13	1.53E+00	1.45E+05	-7.87E-01	-4.41E+04
7	2.97E+14	1.82E+00	9.29E+04	-2.69E+00	1.62E+04

Using the initial parameters provided in Table 3, a curve fit was made of each segment with heating and holding temperatures combined. However, three adjustments were made to properly optimize the fit:

1. Due to the outlying nature of Segment 3's parameters, a linear interpolation was performed on all parameters, which resulted in an acceptable fit.
2. a_5 from the initial segmented fit had to be fixed due to the large variability observed in the final fit.
3. a_5 for Segment 7 had to be changed to the averages of Segment 1-6's a_5. This is because the original parameter as well as the extrapolated value failed the optimization.

With these adjustments made, the individual complete segment fit per Equation (6) was made and given in Table 4.

Table 4. Individual segment fit according to Equation (6).

Segment	a_1	a_2	a_3	a_4	a_5[2]
1	3.65E+13	1.29E+00	--	-6.69E+00	1.89E+04
2	5.68E+11	1.19E+00	--	-1.46E-01	-1.39E+04
3[1]	6.43E+11	1.20E+00	--	-1.68E-01	-2.56E+04
4	1.41E+12	1.27E+00	--	-3.14E-01	-3.72E+04
5	4.67E+12	1.41E+00	--	-7.89E-01	-6.32E+02
6	4.21E+11	1.21E+00	--	-8.27E-01	-4.41E+04
7	2.06E+16	2.16E+00	--	-2.03E+00	-1.12E+03[3]

[1] All initial fit parameters were taken as the average of segment 2 and 4.
[2] Parameter had to be fixed to reduce the number of variables needed to optimize the fit.
[3] The fixed a_5 parameter was taken as the average of segments 1-6.

5. DISCUSSION

5.1 Parameter Comparison with Theory

As shown in Equations (4)–(6), the parameters in Table 4 have theoretical definitions. A qualitative discussion on each parameters is provided below.

a_1 is considered the proportional weighing factor to radiation intensity. While the theory presented in Equation (3) suggests that a_1 is expected to be a constant, an applied field photoconduction model could potentially explain the results. Applied field photoconductivity, σ, can be formalized as [15]:

$$\sigma \propto \left(\frac{R}{T}\right) e^{-\frac{E}{kT}} \tag{7}$$

where

$E > kT$ for a trap-dominated situation such as the crushable mineral insulation.

Here, the formalization requiring the 1/T in Equation (7) necessitates the application of an electric field. This 1/T term was thus dropped in Equation (3) because of the difference in operation. The SPND was not operated with an external voltage applied as in Lynch and Böck [14], [15], but rather from a significantly lesser self-generated electric field. Furthermore, it was observed from Test 1 that when a voltage was applied to measure the resistance on Rh–SPND-1, the signals indicated a strong negative shift when temperature was increased. This suggests that a significant change in space charge distribution within the insulator that is not characteristic of the SPND had occurred because of the applied voltage. However, re-introducing the 1/T formalization to parameter a1 seems to still be applicable. In this case, it would coincide with Böck [15] where photoconductivity reaches a saturation somewhere between 550 and 575°C as shown in Figure 10. After which ionic conduction—which has a similar form with different energy lines—given in Equation (8) takes over until 675°C where another transition, most indicative towards electronic conduction, begins.

$$\sigma = \left(\frac{c}{T}\right) e^{-\frac{\left(E_m + \frac{1}{2}E_f\right)}{kT}} \quad (8)$$

here

E_m = energy for vacancy (ion) migration

E_f = energy for vacancy creation.

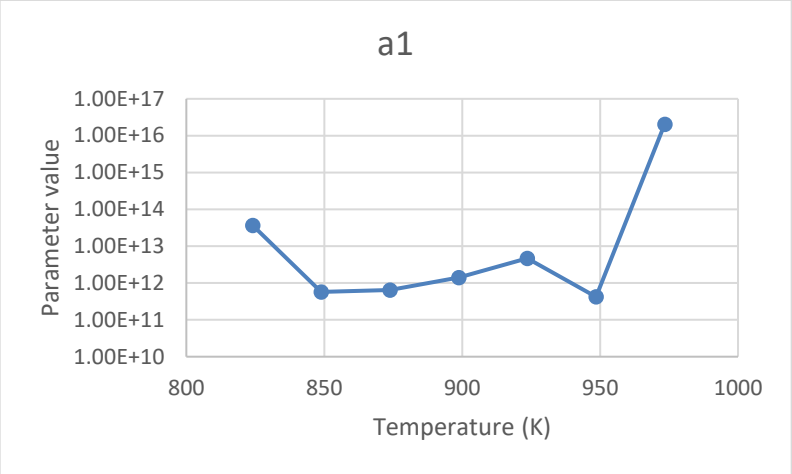

Figure 10. Parameter a_1 vs temperature.

Despite the difference in theory described for a_1, it is assumed that a_2 is unaffected due to the nature functional result of a_1. Therefore, a_2, is still assumed to have a constant value. However, from Figure 11, it is observed that beyond 675°C there is a significant increase in the representation of conductivity. This suggests that a conversion from ionic conduction to electronic conduction (that is estimated to be negligible below 725°C) is potentially visible in the current SPND from 675°C to 700°C. Not only does this increase the displacement current magnitude as a function of temperature, but this transition may also affect higher energy electrons such as those from the (n, β^-) contribution. The average energy of the free electrons exists at similar magnitude resulting in higher conductivity (thus sensitivity), and slower electron motion due to increased collisions between free electrons.

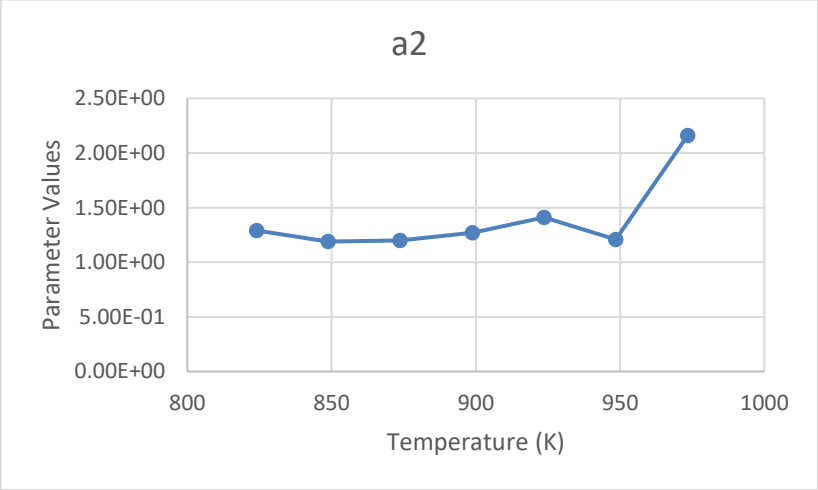

Figure 11. Parameter a_2 vs temperature.

Parameter a_4 represents the decay time constant in relation to temperature. As mentioned, this was an empirical parameter measured by Mitel'man [7] to be linearly proportional to resistance. This provides the proportional relationship $-a_4^{-1} \propto R$ which is expected to decrease exponentially with temperature. However, in Figure 12, this was not the case given the fast decay observed at 550°C This could mean that the recombination rate from photoconduction exceeds the recombination rate from ionic conduction, as discussed in the review of parameter a_1.

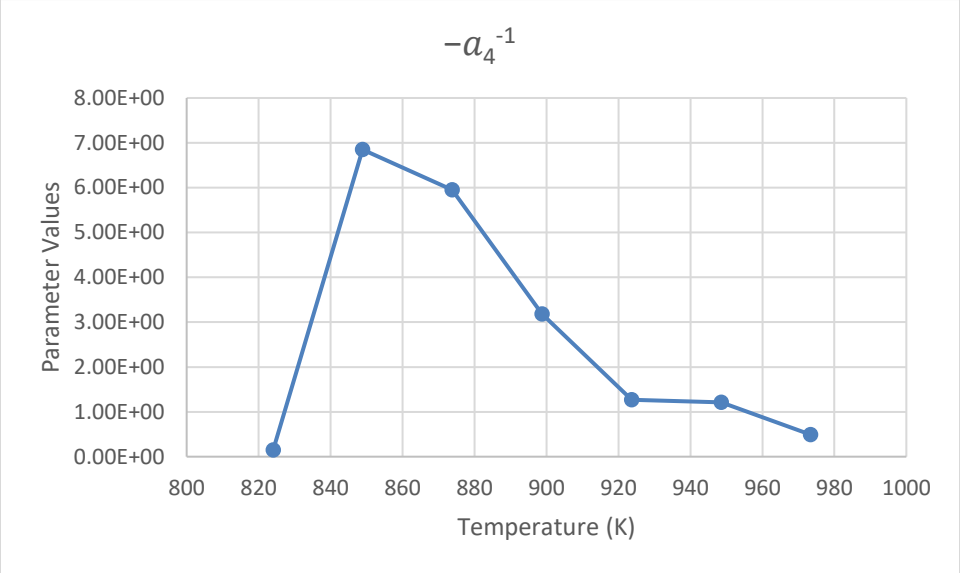

Figure 12. Parameter $-a_4^{-1}$ vs temperature.

Finally, parameter a_5 is viewed as a random spread. This is mostly due to the nature of fixing the parameter during the final fit. Additionally, in the preliminary fit, the data available did not contain the total time to reach stability as the time needed is estimated to be between 0.4 to 11.4-hour holds which was outside of the available irradiation time.

Given the insight provided by the parameters above, there are potentially two transition points observed—one near 550°C and the other near 700°C While these two points coincide in the ranges also provided by Böck [15], these values less suggest transitions between different impurity values of E_m and E_f, but rather the transition from photoconductivity to ionic conductivity to electronic conductivity.

5.2 Considerations for Future Work

While the parameters measured within this work provided some useful insight into the behavior of sensitivities as pertained to (n, β^-) interactions and (n, γ, e) interactions with increasing temperature, there are many missing data points for full application to a temperature compensation algorithm. This is largely due to the unavailable data at the transition points near 550°C and 700°C, as well as the final decayed dark current, a_5, that would reduce the uncertainty of the curve-fit parameters. Some considerations for future work to improve on the measurements performed within this project would be:

1. Increase the temperature hold points, specifically near the transition points. This includes changing the range of temperature ramps or varying steady-state duration to investigate any limits in trapping and releasing electrons.
2. Increase the irradiation time to accurately account for decay time constant as well as the stabilized dark current.
3. A new conductivity model needs to be created based on a self-generated electric field.

All three of these properties can be investigated in a gamma irradiation facility. However, to further understand the effects of the higher temperature conduction properties involving higher-energy electrons from (n, β^-) reactions, neutron irradiations will be needed.

6. REFERENCES

[1] IAEA. 1999. "Technical Reports Series No. 387: Modern Instrumentation and Control for Nuclear Power Plants: A Guidebook." International Atomic Energy Agency. https://www.iaea.org/publications/5721/modern-instrumentation-and-control-for-nuclear-power-plants.

[2] U.S. NRC . n.d. "Westinghouse Technology Systems Manual." U.S. Nuclear Regulatory Commission Human Resources Training & Development, Section 9.2 Incore Instrumentation System, rev. 0404. https://www.nrc.gov/docs/ML1122/ML11223A264.pdf.

[3] U.S. DOE. 2015. "Quadrennial Technology Review 2015 High Temperature Reactors Chapter 4: Technology Assessments." U.S. Department of Energy. https://www.energy.gov/sites/default/files/2016/03/f30/QTR2015-4J-High-Temperature-Reactors.pdf.

[4] Lewis, R. H. 1967. "All-solid In-core Power Monitors for LMBFR Service." *Proceedings of the Symposium on Liquid Metal Instrumentation and Control*, ANL-7380, 140—145. https://doi.org/10.2172/4496346.

[5] Tsai, K., Palmer, J., and Reichenberger. M. A. 2021. "Comparative Assessment of Neutron Flux Sensor Technologies for Advanced Reactors." INL/EXT-21-65635, Idaho National Laboratory. https://inldigitallibrary.inl.gov/sites/sti/sti/Sort_56134.pdf.

[6] Tsai, K. 2022. "Development of Temperature Compensation Tools for SPNDs Operating in High Temperature Environments." INL/RPT-22-69883, Idaho National Laboratory. https://inldigitallibrary.inl.gov/sites/sti/sti/Sort_64124.pdf.

[7] Mitel'man, M.G., et al. 1980. "Effect of temperature on characteristic of self-powered detectors. At Energy, (48): 263—266. https://doi.org/10.1007/BF01146664.

[8] Warren, H. D. and Shah, N. H. 1974. "Neutron and Gamma-Ray Effects on Self Powered In-Core Radiation Detectors." *Nuclear Science and Engineering*, (54)4: 395—415. https://doi.org/10.13182/NSE74-A23434.

[9] OSU COE. n.d. "6.5-inch External Dry Tube Neutron Spectrum Measurement." Ohio State University, College of Engineering, NRL-2020-19 rev. 1.

[10] Valentine, T. E. 2001. "MCNP-DSP Users Manual." ORNL/TM-13334, R2. Oak Ridge National Laboratory. https://info.ornl.gov/sites/publications/Files/Pub57086.pdf.

[11] Goldstein, N. P. 1973. "A Monte-Carlo Calculation of the Neutron Sensitivity of Self-Powered Detectors." *IEEE Transactions on Nuclear Science*, (20)1: 549—556. https://ieeexplore.ieee.org/document/4326961.

[12] Warren, H. D. 1972. "Calculational Model for Self-Powered Neutron Detector." *Nuclear Science and Engineering*, (48)3: 331—342. https://doi.org/10.13182/NSE72-A22491.

[13] Kittel, C. 1956. "Introduction to Solid State Physics." 2nd ed., John Wiley & Sons, Inc., New York.

[14] Lynch, G. F. and Shields, R. B. 1974. "On the Use of MgO As Insulation for Coaxial Signal Cables in a Reactor Environment." AECL-4827, Atomic Energy of Canada Limited, Chalk River Nuclear Laboratories. https://inis.iaea.org/collection/NCLCollectionStore/_Public/06/158/6158764.pdf.

[15] Böck, H. and Suleiman, M. 1978. "Investigations of mineral insulated cables exposed to high temperature and intense gamma radiation." *Nuclear Instruments and Methods*, (148)1: 43—50, 1978. https://doi.org/10.1016/0029-554X(78)90333-6.